

# Formation and evolution of the water maser outflow event in AFGL 2591 VLA 3-N

M. A. Trinidad<sup>1\*</sup>, S. Curiel<sup>2</sup>, R. Estalella<sup>3</sup>, J. Cantó<sup>2</sup>, A. Raga<sup>4</sup>,  
J. M. Torrelles<sup>5</sup>, N. A. Patel<sup>6</sup>, J. F. Gómez<sup>7</sup>, G. Anglada<sup>7</sup>,  
C. Carrasco-González<sup>8</sup>, L. F. Rodríguez<sup>9</sup>

<sup>1</sup>*Departamento de Astronomía, Universidad de Guanajuato, Apdo. Postal 144, 36000 Guanajuato, México*

<sup>2</sup>*Instituto de Astronomía (UNAM), Apartado 70-264, 04510 México D. F., México*

<sup>3</sup>*Departament d'Astronomia i Meteorologia and Institut de Ciències del Cosmos (IEEC-UB), Universitat de Barcelona, Martí i Franquès 1, 08028 Barcelona, Spain*

<sup>4</sup>*Instituto de Ciencias Nucleares (UNAM), Apartado 70-543, 04510 México D. F., México*

<sup>5</sup>*Instituto de Ciencias del Espacio (CSIC)-UB/IEEC, Universitat de Barcelona, Martí i Franquès 1, 08028 Barcelona, Spain*

<sup>6</sup>*Harvard-Smithsonian Center for Astrophysics, 60 Garden Street, Cambridge, MA 02138, USA*

<sup>7</sup>*Instituto de Astrofísica de Andalucía (CSIC), Apartado 3004, 18080 Granada, Spain*

<sup>8</sup>*Max-Planck-Institut für Radioastronomie (MPIfR), Auf dem Hügel 69, 53121 Bonn, Germany*

<sup>9</sup>*Centro de Radioastronomía y Astrofísica (UNAM), 58089 Morelia, México*

Accepted 2012 December 21. Received 2012 December 20; in original form 2012 November 5

## ABSTRACT

In this paper we analyze multi-epoch Very Long Baseline Interferometry (VLBI) water maser observations carried out with the Very Long Baseline Array (VLBA) toward the high-mass star-forming region AFGL 2591. We detected maser emission associated with the radio continuum sources VLA 2 and VLA 3. In addition, a water maser cluster, VLA 3-N, was detected  $\sim 0.5''$  north of VLA 3. We concentrate the discussion of this paper on the spatio-kinematical distribution of the water masers towards VLA 3-N. The water maser emission toward the region VLA 3-N shows two bow shock-like structures, Northern and Southern, separated from each other by  $\sim 100$  mas ( $\sim 330$  AU). The spatial distribution and kinematics of the water masers in this cluster have persisted over a time span of seven years. The Northern bow shock has a somewhat irregular morphology, while the Southern one has a remarkably smooth morphology. We measured the proper motions of 33 water maser features, which have an average proper motion velocity of  $\sim 1.3$  mas yr<sup>-1</sup> ( $\sim 20$  km s<sup>-1</sup>). The morphology and the proper motions of this cluster of water masers show systematic expanding motions that could imply one or two different centers of star formation activity. We made a detailed model for the Southern structure, proposing two different kinematic models to explain the 3-dimensional spatio-kinematical distribution of the water masers: (1) a static central source driving the two bow-shock structures; (2) two independent driving sources, one of them exciting the Northern bow-shock structure, and the other one, a young runaway star moving in the local molecular medium exciting and molding the remarkably smoother Southern bow-shock structure. Future observations will be necessary to discriminate between the two scenarios, in particular by identifying the still unseen driving source(s).

**Key words:** ISM: individual (AFGL 2591) — ISM: jets and outflows — masers — stars: formation

\* E-mail: trinidad@astro.ugto.mx (MAT);  
scuriel@astrocu.unam.mx (SC); robert@am.ub.es (RE); torrelles@ieec.cat (JMT); npatel@cfa.harvard.edu (NAP); jfg@iaa.es

(JFG); guillem@iaa.es (GA); carrasco@mpifr-bonn.mpg.de (CC-G); raga@nucleares.unam.mx (ACR); l.rodriguez@crya.unam.mx (LFR)

## 1 INTRODUCTION

In the last few decades great progress has been made in the understanding of how low-mass stars form, through multi-wavelength observations and detailed theoretical models. It is now relatively well understood that during the early stages of evolution of low-mass stars, a system is formed with a central protostar, surrounded by a rotating accretion disk at scales of  $\sim 100$  AU, and ejecting a highly collimated jet along the polar axis of the disk. While the disk is the reservoir from which the protostar accretes further matter, the ejected outflow removes angular momentum and magnetic flux from the system, allowing the accretion to proceed until the central star is assembled (e.g., Lada 1995; McKee & Ostriker 2007; Machida, Inutsuka & Matsumoto 2008; Armitage 2011; Williams & Cieza 2011). However, the processes that give rise to massive stars ( $\gtrsim 8 M_{\odot}$ ) are still not well understood. Several well differentiated mechanisms for forming massive stars have been proposed. For example, via an accretion disk (as low-mass stars, but with a higher accretion rate), via competitive accretion in a proto-cluster environment, or via mergers in very dense systems of lower mass stars (Bally & Zinnecker, 2005). Distinguishing between these possible scenarios is a very difficult observational task, essentially because massive young stars are rare and more distant compared to low-mass young stars. Furthermore, massive stars form in clusters in highly obscured regions, making it difficult to identify individual massive young stellar objects (YSOs) for detailed studies (see, e.g., Hoare & Franco 2007; Hoare et al. 2007; Zinnecker & Yorke 2007 and references therein). In this sense, recent interferometer observations at cm and (sub)mm wavelengths with angular resolutions of  $\sim 0.1''$  ( $\sim 100$  AU at 1 kpc distance) suggest that stars with masses at least up to  $\sim 20 M_{\odot}$  may form via the accretion disk scenario, in a similar way as low-mass stars do, although the number of massive disk-protostar-jet systems identified and studied at scales of  $\sim 1000$  AU is still very small (e.g., Patel et al. 2005; Jiménez-Serra et al. 2007; Torrelles et al. 2007; Zapata et al. 2009; Davies et al. 2010; Carrasco-González et al. 2010, 2012; Fernández-López et al. 2011).

Within this context, observations of maser transitions of several molecular species (e.g.,  $H_2O$ , OH,  $CH_3OH$ ) in the proximity of high-mass protostellar objects (HMPOs) provide a powerful diagnostic tool to investigate the first stages of the evolution of massive star formation (e.g., Sanna et al. 2010a,b; Bartkiewicz & van Langevelde 2012). In particular, the use of Very Long Baseline Interferometry (VLBI) techniques for observing maser emission with angular resolution  $\lesssim 1$  mas ( $\lesssim 1$  AU at 1 kpc distance), allows us to study some of the main properties of the densest and hence most obscured portions of molecular clouds where the new massive stars are born. In addition, it is possible to derive the three-dimensional (3D) velocity distribution of the masing gas very close to HMPOs (e.g., Goddi et al. 2006; Matthews et al. 2010; Goddi, Moscadelli & Sanna 2011; Torrelles et al. 2011; Chibueze et al. 2012), and through polarization measurements, the distribution and strength of the magnetic field in the cores of star forming regions (e.g., Vlemmings et al. 2006, 2010; Surcis et al. 2011a,b, 2012). Moreover, the detection of outflow activity by means of VLBI maser observations also allows us to identify new, previously unseen

centers of massive star formation, some of them associated with unexpected phenomena such as “short-lived” episodic ejection events characterized by kinematic ages of a few tens of years in the earliest stages of evolution of HMPOs (Torrelles et al. 2001, 2003, 2011; Gallimore et al. 2003; Surcis et al. 2011a; Chibueze et al. 2012; Sanna et al. 2012).

AFGL 2591 is one of the most extensively studied high-mass star-forming regions in our Galaxy (e.g., van der Tak et al. 2006; Jiménez-Serra et al. 2012 and references therein). Located in the Cygnus X region, its distance has been recently estimated as  $3.33 \pm 0.11$  kpc, via measurements of trigonometric parallax of masers (Rygl et al. 2012). It appears completely obscured at optical wavelengths, but it has a very high luminosity in the infrared (IR) ( $L_{\text{bol}} \simeq 2 \times 10^5 L_{\odot}$ ; Sanna et al. 2012). Three radio continuum sources have been detected toward AFGL 2591 within an area of  $\sim 6'' \times 6''$  ( $\sim 0.1$  pc), VLA 1, VLA 2, and VLA 3 (Campbell 1984; Trinidad et al. 2003). Of these, VLA 3 is believed to be the youngest ( $\sim 2 \times 10^4$  yr; Tofani et al. 1995; Doty et al. 2002; Stäuber et al. 2005) and more massive object (mass in the range 20-38  $M_{\odot}$ ), dominating the IR emission of the region (Sanna et al. 2012). Submillimeter Array (SMA) observations carried out by Jiménez-Serra et al. (2012) show that VLA 3 is surrounded by a hot molecular core and that the global kinematics of the molecular gas is consistent with Keplerian-like rotation around a central source of  $\sim 40 M_{\odot}$ . In addition, a powerful molecular outflow aligned along the east-west direction has been observed in the region (Bally & Lada 1983; Torrelles et al. 1983; Lada et al. 1984; Mitchell, Maillard & Hasegawa 1991), with VLA 3 being its most likely driving source candidate (Trinidad et al. 2003). On the other hand, VLA 1 and VLA 2 are optically thin HII regions excited by early B-type stars (Trinidad et al. 2003).

Water maser emission is observed toward this massive star forming region, mainly associated with sources VLA 2 and VLA 3 (Tofani et al. 1995; Trinidad et al. 2003). Trinidad et al. (2003) detected with the Very Large Array (VLA; beam size  $\simeq 0.08''$ ) two well-differentiated clusters of water masers in the vicinity of VLA 3, one peaking at (and probably excited by) this massive YSO, and the other located  $\sim 0.5''$  ( $\sim 1600$  AU) north from it (see Figure 1). These authors suggest that the latter cluster is excited by an independent, still undetected embedded YSO located  $\sim 0.5''$  north from VLA 3. This interpretation has been recently supported by Sanna et al. (2012) with VLBI multi-epoch water maser observations (angular resolution of 0.6 mas), which show that the cluster of masers to the north of VLA 3 is formed by two bow shock-like structures separated  $\sim 0.12''$  ( $\sim 400$  AU), and moving away from each other along a north-south direction with proper motions of  $\sim 20 \text{ km s}^{-1}$ . Sanna et al. propose that a still undetected central massive protostar(s) (probably a late B-type star, based on the luminosity of the masers) is ejecting a jet that generates the two bow shocks at its tips. The short kinematic age of the expanding motions traced by the water masers (few tens of years) also led these authors to suggest that they are probably the result of recurrent pulsed jet events rather than of a steady jet from the central protostar(s). Therefore, this could represent an important new case providing indications that massive objects are characterized by recurrent outflow

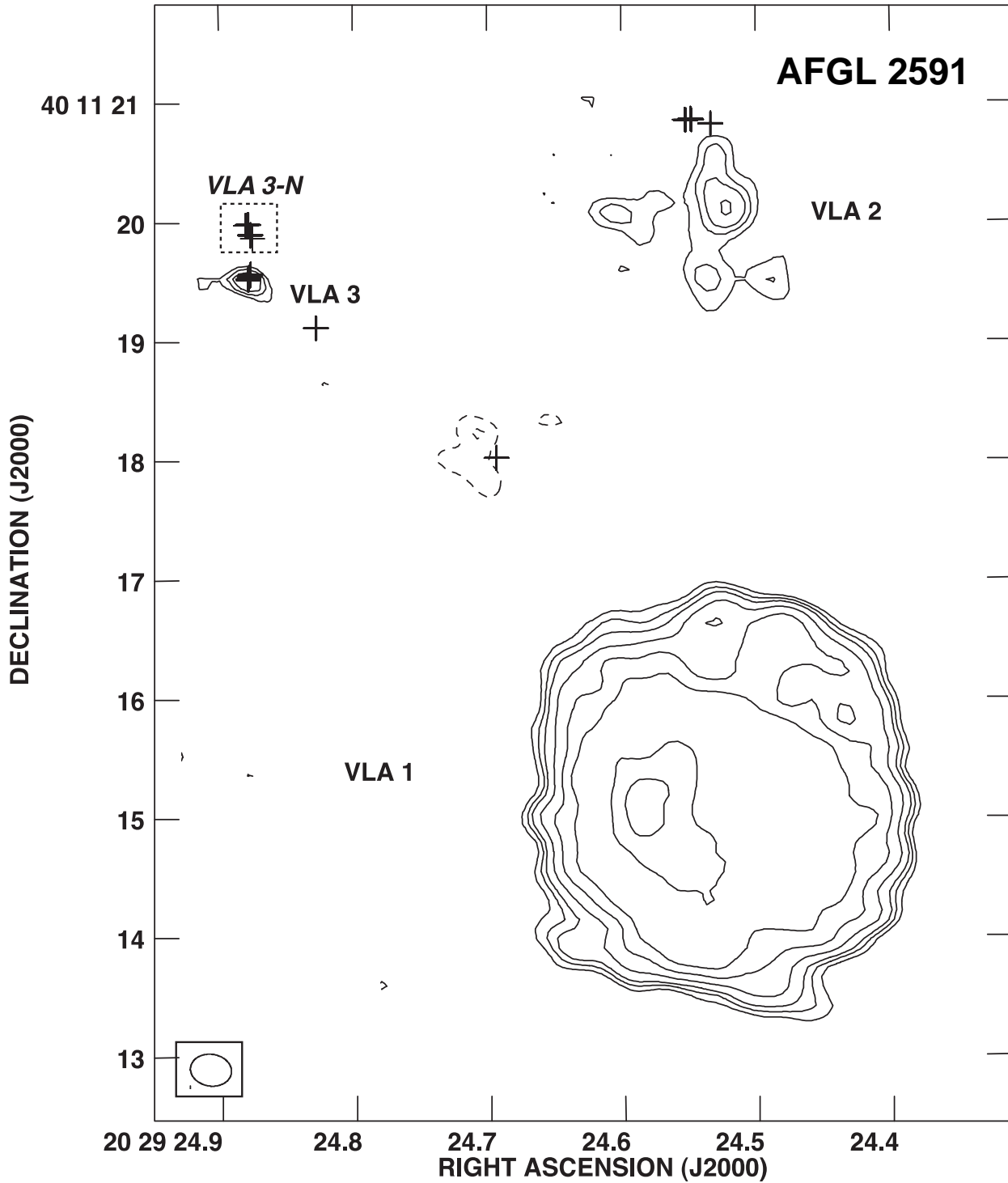


**Figure 1.** VLA 3.6 cm continuum contour map of the high-mass star forming region AFGL 2591, showing the radio continuum sources VLA 1, VLA 2, and VLA 3, all of them excited by massive stars (see §1). Plus symbols indicate the positions of the VLA 22 GHz water masers detected in the region (figure from Trinidad et al. 2003). The region analyzed and discussed in this paper is VLA 3-N (enclosed by a dashed square), located  $\sim 0.5''$  north of VLA 3. This is the region where Trinidad et al. (2003) proposed that an internal source other than VLA 3 is exciting these water masers.

events during the early stages of their evolution (e.g. Martí et al 1995; Curiel et al. 2006).

In this paper we present (§2) VLBI multi-epoch water maser data observed toward AFGL 2591, about 7 years before (2001-2002 epochs) than those observed by Sanna et al (2012) (2008-2009 epochs). Our data show a water maser spatio-kinematical distribution that is globally consistent with that reported from the 2008-2009 epoch data, but less extended and smoother. We analyze the 3-D kinematical and spatial distribution of the maser structures following their evolution during the time span of 7 years (§3), modeling the formation and evolution of these maser structures in terms of two possible scenarios: (1) a single static central massive YSO, ejecting a jet driving the two bow-shock maser structures; (2) two embedded driving sources, one exciting the northern bow shock, and the other one a young runaway star moving in the local medium at  $\sim 20 \text{ km s}^{-1}$  and exciting the smoother southern bow-shock structure observed in our data (§4). The main conclusions are presented in §5.

## 2 OBSERVATIONS

Multi-epoch water maser observations were carried out with the Very Long Baseline Array (VLBA) of the National Radio Astronomy Observatory (NRAO)<sup>1</sup> toward AFGL 2591 at three epochs (2001 December 2, 2002 February 11, and 2002 March 5). We observed the  $6_{16} - 5_{23}$  water maser transition (rest frequency = 22235.08 MHz) with a bandwidth of 8 MHz sampled over 512 channels (spectral resolution  $15.625 \text{ kHz} = 0.21 \text{ km s}^{-1}$ ) and centered at  $V_{\text{LSR}} = -7.6 \text{ km s}^{-1}$ . All ten VLBA stations of the array were available and recorded data during an observing time of 6 hours per epoch. The data were correlated at the NRAO Array Operation Center.

The amplitude and phase calibration of the observed visibilities, as well as further imaging, were made with the NRAO Astronomical Image Processing System (AIPS) package. The sources 3C45, B2007+777, BL Lac, and 3C454.3 were used for delay and phase calibration, while bandpass corrections were made using 3C345, BL Lac, and 3C454.3. An isolated maser spot, with a point-like morphology and with high intensity ( $\simeq 10 \text{ Jy}$ ) in all three epochs, was chosen to self-calibrate the data and to obtain a first and preliminary coordinate alignment between the three observed epochs. This reference maser spot has a radial velocity of  $V_{\text{LSR}} = -18.8 \text{ km s}^{-1}$  and it is located toward VLA 3, with absolute coordinates  $\alpha(\text{J2000.0}) = 20^{\text{h}}29^{\text{m}}24.879^{\text{s}}$ ,  $\delta(\text{J2000.0}) = 40^{\circ}11'19.47'' (\pm 0.01'')$ .

As a first step to identify the subregions of AFGL 2591 with water maser emission, we produced large maps with low angular resolution for each of the three observed epochs. These maps had  $8192 \times 8192$  pixels of 1 mas each, over 512 velocity channels, covering a region of  $8.2'' \times 8.2''$  centered on the reference maser spot. From them, three subregions with maser emission were identified, one associated with VLA 2, another with VLA 3, and the third one located  $\sim 0.5''$  north of VLA 3. We did not detect maser emission in the region

$\sim 2''$  southwest of VLA 3, where water maser emission was previously identified with the VLA (Trinidad et al. 2003; see Figure 1). We then obtained simultaneously, for each epoch, full-resolution maps ( $8192 \times 8192$  pixels of 0.1 mas each, over 512 channels) of these fields, as well as of an additional subregion where Sanna et al. (2012) also identified water maser emission (the subregion named in that paper as MW, and located  $\sim 0.6''$  west of VLA 3). The resulting synthesized beam size was  $\sim 0.45 \text{ mas}$  for the three observed epochs. The rms noise level of the maps ranges from  $\sim 5 \text{ mJy beam}^{-1}$  in the channel maps with weak signal, to  $\sim 250 \text{ mJy beam}^{-1}$ , in the channels with the strongest maser components.

Finally, each velocity channel map was searched for maser spots. We refer to a maser spot as emission that occurs at a given velocity channel and with a distinct spatial position. The threshold for the maser spot detection was taken to be equal to  $10 \sigma$  in each velocity channel, using the maser spot search procedure described in Surcis et al. (2011a). Clusters of maser spots were detected in the subregions around VLA 2, VLA 3, and  $\sim 0.5''$  north of VLA 3. We did not detect any emission in the MW region, where Sanna et al. (2012) found water maser emission about seven years later. We fitted all the maser spots detected with two-dimensional elliptical Gaussians, determining their position, flux density, and radial velocity. The water maser emission in the AFGL 2591 region spans a velocity range from  $V_{\text{LSR}} \simeq -31$  to  $-2 \text{ km s}^{-1}$ . We estimated that the  $1\sigma$  accuracy in the relative positions of the maser spots at each epoch is better than  $\sim 0.01 \text{ mas}$  ( $\text{beam}/[2 \times \text{SNR}]$ ; Meehan et al. 1998). In this paper, we will concentrate on the spatio-kinematical distribution of the masers found  $\sim 0.5''$  north of VLA 3 (hereafter VLA 3-N), where Sanna et al. (2012) identified two bow-shock like structures (see §1). The other two observed clusters of masers associated with VLA 2 and VLA 3 will be presented and discussed elsewhere.

In Table A1 (published online) we list the positions, LSR radial velocity, and intensity of all the maser spots detected in the region VLA 3-N for the three observed epochs. From this list of maser spots (Table A1) we identified maser features for proper motion measurements purposes. We refer to a maser feature as a group of three or more maser spots coinciding within a beam size ( $\sim 0.4 \text{ mas}$ ), and each of them appearing in consecutive velocity channels ( $0.21 \text{ km s}^{-1}$ ). Table 1 contains the main parameters of the 33 maser features from which we measured proper motions using the three observed epochs (02Dec2001, 11Feb2002, and 05Mar2002). For the alignment of our three observed epochs with the data set of Sanna et al (2012) to make a proper comparison (main goal of this work), we identify a maser feature clearly persisting in the two sets of data: S 17 listed by Sanna et al. (2012) (which has a relatively small proper motion), identified in our data set as maser feature ID28 (both having similar radial velocities; Tables 1 and 2). We have corrected the positions of the feature ID 28 as a function of time (and therefore to all our data set of 2001-2002), extrapolated from the position and proper motion of the maser S17 (Sanna et al. 2012), assuming that it has moved with constant velocity through the time span of  $\sim 7 \text{ yr}$ . After this alignment, proper motions listed in Table 1 were estimated by a linear fitting to position of the masers of the three different epochs as a function of time. The fact that after this alignment, the whole maser structure of our obser-

<sup>1</sup> The NRAO is a facility of the National Science Foundation operated under cooperative agreement by Associated Universities, Inc.

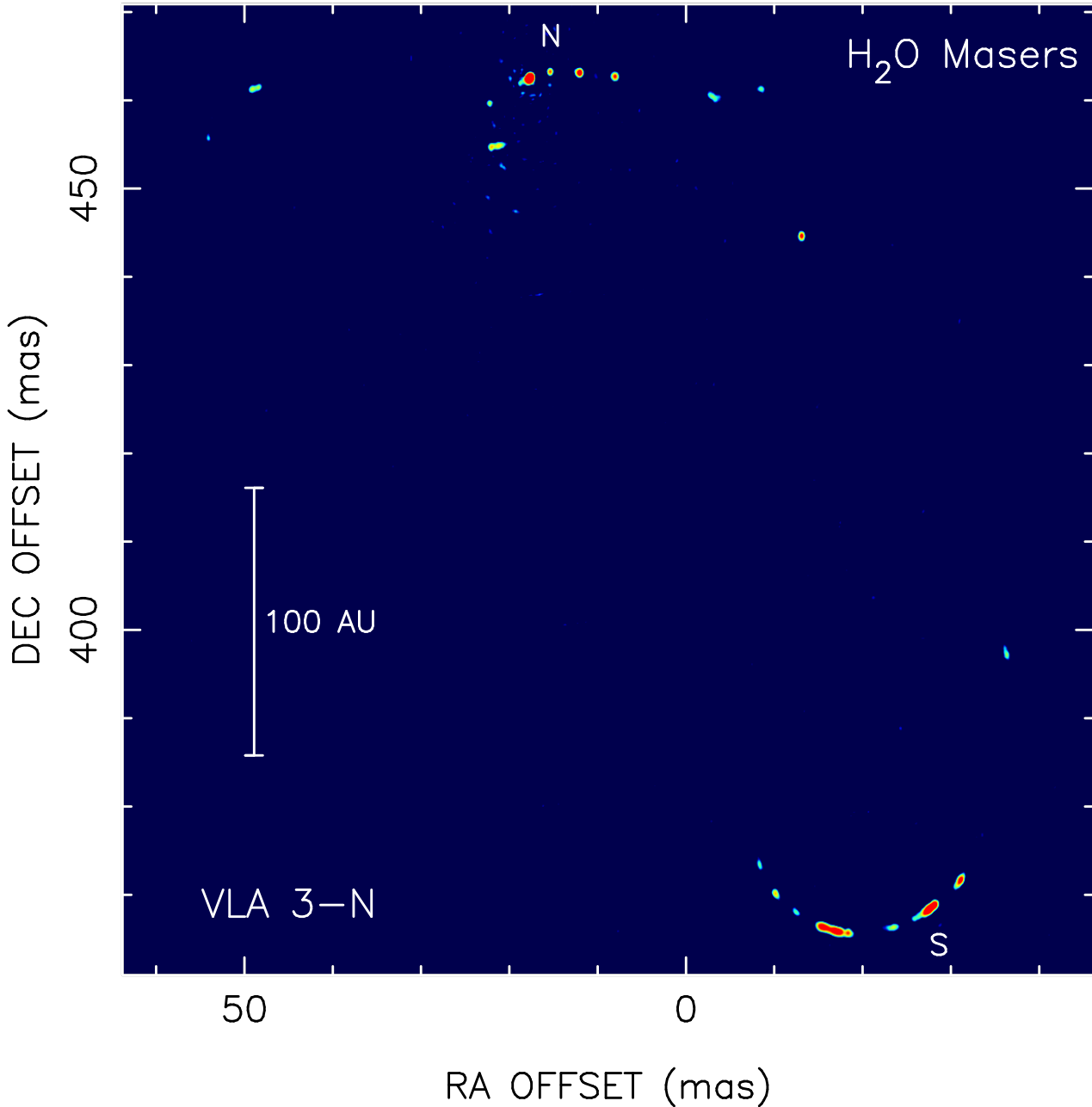


**Figure 2.** Integrated intensity image of the water maser emission in the region VLA 3-N (dashed square in Figure 1) for the first epoch of the VLBA observations on 2001 Dec 2 (the spatial distribution of the water maser emission is very similar in the two other observed epochs, 2002 Feb 11 and 2002 Mar 5). The colour intensity scale is saturated at  $7 \text{ Jy beam}^{-1}$  (beam  $\simeq 0.45 \text{ mas}$ ) to show the full water emission structure. The intensity of all the water masers spots is listed in Table A1 (published online).

variations is within that reported by Sanna et al. (2012), and that the estimated shift in position of our observed masers for a time span of seven years coincide with the angular separation between the structures observed in 2001-2002 (this paper) and those of 2008-2009 (Sanna et al. 2012) (see below, §3) gives our alignment and proper motion estimates an additional measure of robustness.

We note that the maser feature ID 28 is not the maser used to self-calibrate our data, which is associated with the radio continuum source VLA 3 ( $\sim 0.5''$  south of VLA 3). All the offset positions of the masers given in this paper

(tables and figures) are relative to the maser spot position (0,0) used for self-calibrating the data of our first epoch of observations (02Dec2001; see above). For comparison purposes, further analysis, and full discussion of all the results obtained in this region, we also list in Table 2 the 19 water maser features where proper motions have been measured by Sanna et al. (2012) for the 2008-2009 epochs in VLA 3-N (all the positions listed in Table 2 are also given with respect to our reference position  $[0,0]$ ,  $\alpha$  [J2000] =  $20^{\text{h}}29^{\text{m}}24.879^{\text{s}}$ ,  $\delta$  [J2000] =  $40^{\circ}11'19.47'' \pm 0.01''$ ).

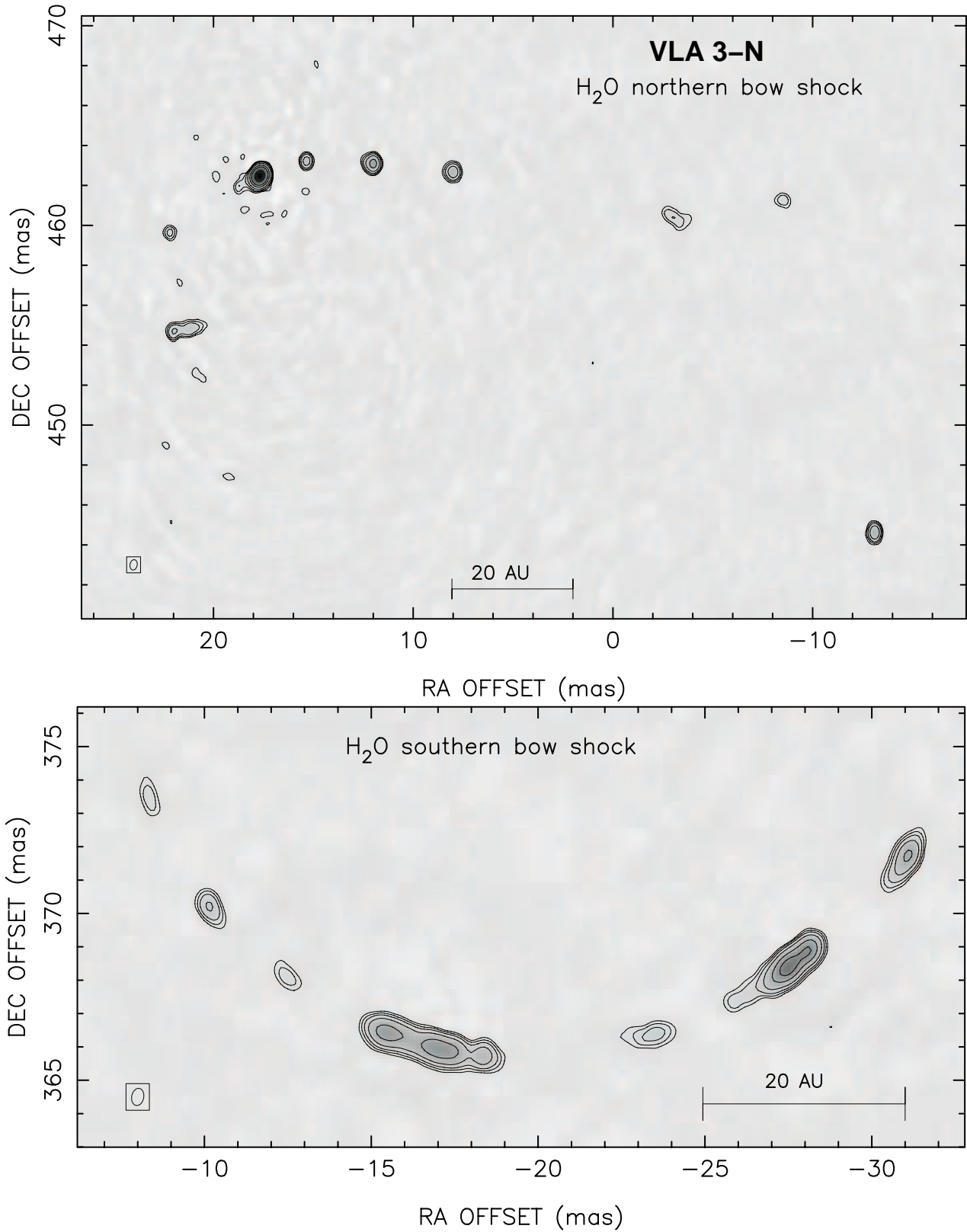


**Figure 3.** Close up of the integrated water maser emission in VLA 3-N (shown in Figure 2) for the Northern (upper panel) and Southern (lower panel) bow-shock structures for the first epoch of the VLBA observations on 2001 Dec 2 (the spatial distribution of the water maser emission is very similar in the two other observed epochs, 2002 Feb 11 and 2002 Mar 5). Contours levels are 0.7, 1.2, 2, 4, 10, 20, 60 Jy beam<sup>-1</sup> (beam  $\simeq$  0.45 mas).

### 3 OBSERVATIONAL RESULTS

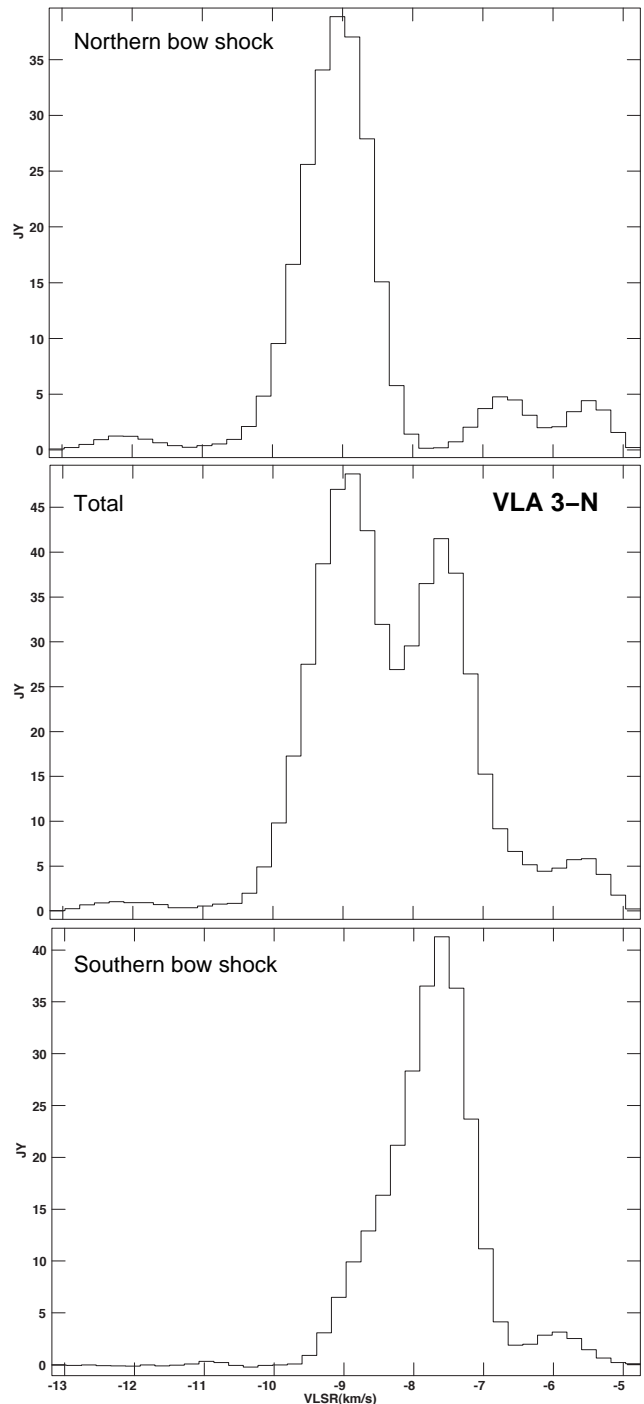
In Figure 2 we present an integrated intensity image of the water maser emission obtained from our VLBA data toward the region VLA 3-N. The emission shows the presence of two shell-like structures of water masers with sizes  $\sim 30$  mas ( $\sim 100$  AU) that resemble bow shocks, named hereafter as the *Northern* and *Southern* bow-shock structures. These structures are observed in our three epochs of observations (2001-2002). The Northern and Southern bow shocks are separated from each other by  $\sim 100$  mas ( $\sim 330$  AU). It is worth noting that the spatial distribution of these water maser structures agrees very well with those traced by the VLBA observations reported by Sanna et al. (2012), made seven years after our observations (see below). This result implies that both the surrounding interstellar medium and the exciting source(s) of the masers have been relatively stable over this temporal scale of seven years.

The Northern and Southern bow shocks detected with our VLBA data present significant morphological differences. In fact, while the Northern bow shock has a somewhat irregular morphology, the Southern one has a remarkable smooth morphology (not so evident in the data presented by Sanna et al. 2012), which has remained stable during our three epochs of VLBA observations. This is more clearly seen in Figure 3, where we show, as close ups, the integrated intensity contour maps of the two bow-shock structures.

The water maser emission in VLA 3-N spans a velocity range from  $V_{\text{LSR}} \simeq -13$  to  $-2$  km s $^{-1}$ , and flux densities range from  $\sim 0.05$  to 30 Jy beam $^{-1}$  (Tables A1 and 1). Most of the water maser emission appears blueshifted with respect to the systemic velocity of the extended ambient molecular cloud of the AFGL 2591 massive star formation region ( $V_{\text{LSR}} \simeq -6$  km s $^{-1}$ ; van der Tak et al. 1999). However, the center of the velocity range covered by the masers is closer to the LSR velocity of the HC $_3$ N line emission from the hot molecular core in VLA 3 ( $V_{\text{LSR}} \simeq -7$  to  $-8$  km s $^{-1}$ ), measured with the SMA with angular resolution  $\sim 0.4''$  (Jiménez-Serra et al. 2012). The water maser spectrum of the whole VLA 3-N region is dominated by two main velocity components ( $\sim 40$  Jy), at  $V_{\text{LSR}} \simeq -9.0$  and  $-7.5$  km s $^{-1}$ , arising from the Northern and Southern bow-shock structures, respectively (see Figure 4).

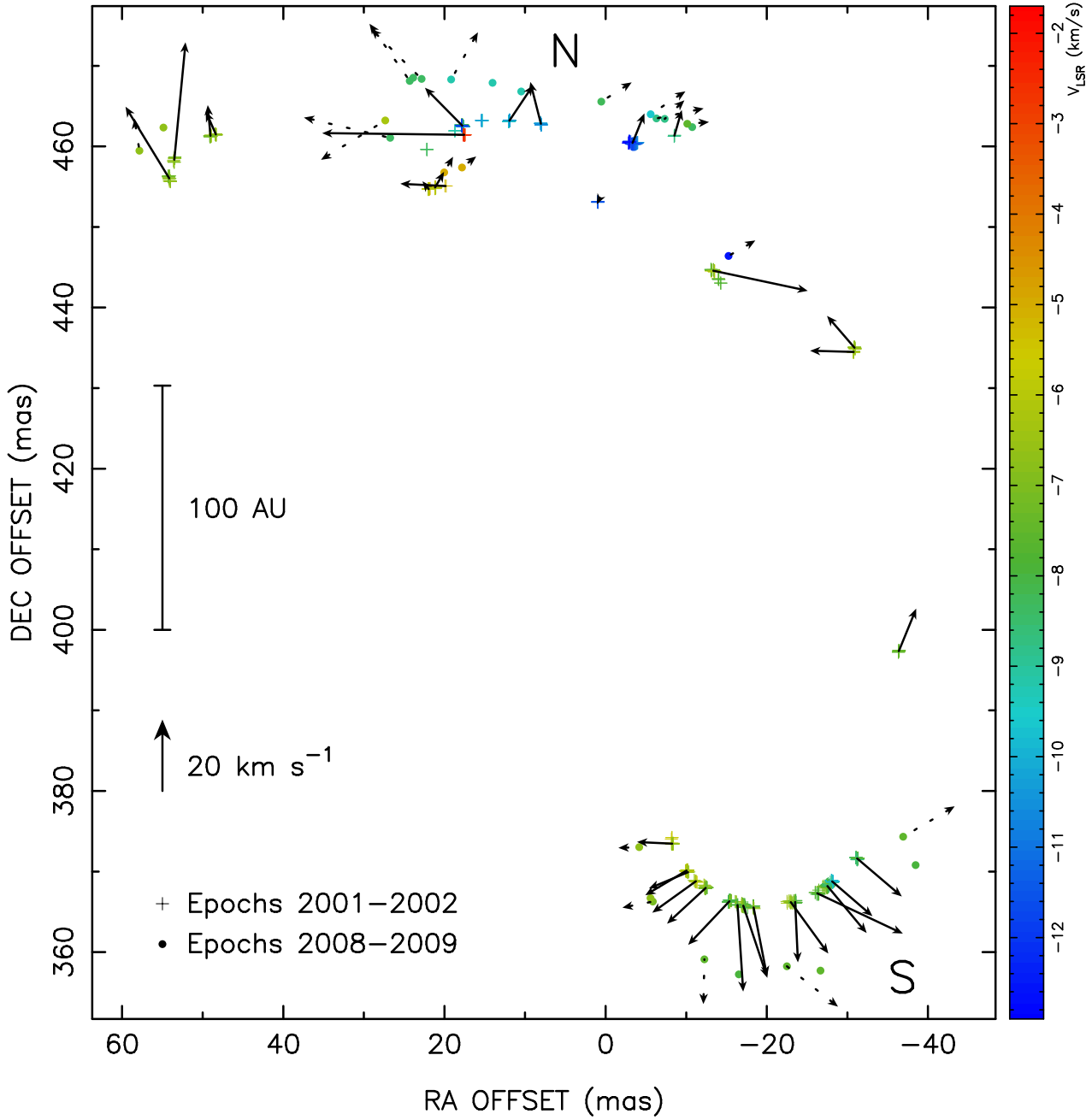
We measured the proper motions of 33 water maser features located in the VLA 3-N region (Table 1), resulting in average tangential velocities of  $\sim 20$  km s $^{-1}$  ( $\sim 1.3$  mas yr $^{-1}$ ). In Figure 5 we plotted the positions of all the water maser spots measured with the VLBA at epochs 2001-2002 (Table A1), together with the proper motion vectors of these 33 maser features (Table 1). We also plotted in this figure the 19 maser features measured by Sanna et al. (2012) in 2008-2009, as well as their proper motions. The color scale of the symbols represent their LSR radial velocities.

Figure 5 shows that the northern masers of VLA 3-N are moving essentially northward, while the southern masers are moving southward (epochs 2001-2002). This is fully consistent with the results reported by Sanna et al. (2012) for epochs 2008-2009. In addition, we found that the two main water maser structures detected in epochs 2001-2002 in VLA 3-N (i.e., the Northern and Southern bow shocks) fall within the corresponding structures observed in epochs



**Figure 4.** Water maser spectra of the Northern (top panel) and Southern (bottom panel) bow-shock structures observed with the VLBA toward VLA 3-N (see Figures 1 and 2) on 2001 December 02 (the spectra in the other two observed epochs are similar). The total spectrum obtained for the full region VLA 3-N ( $\sim 0.1''$  size) is also shown (central panel).

2008-2009. In fact, the Northern and Southern bow-shock structures are separated from each other by  $\sim 100$  mas ( $\sim 330$  AU) in epochs 2001-2002, while they are separated  $\sim 120$  mas ( $\sim 400$  AU) in epochs 2008-2009. This implies that the two bow-shock structures have increased their angular separation in the time span of seven years at a relative proper



**Figure 5.** Positions of all the water maser spots measured with the VLBA in the region VLA 3-N in epochs 2001-2002 (plus signs; this paper, Table A1) and in epochs 2008-2009 (filled circles; Sanna et al. (2012)). The color scale represents the LSR radial velocity of the masers. Arrows (solid and dashed lines for epochs 2001-2002 and 2008-2009, respectively) represent the proper motion vectors of the maser features listed in Tables 1 and 2. The length of the arrows corresponds to the estimated proper motions over the total time span of seven years (time span between our VLBA observations and those of Sanna et al. 2012). Note that the positions of all the maser spots detected in 2001-2002 fall within the area circumscribed by the masers detected in 2008-2009. The Northern and Southern bow-shock structures are separated from each other by  $\sim 100$  mas ( $\sim 330$  AU) for epochs 2001-2002, and  $\sim 120$  mas ( $\sim 400$  AU) for epochs 2008-2009 (see §§3.4).

motion of  $\sim 2.8$  mas yr $^{-1}$ . If we assume expansion from a common center, this would correspond to expanding proper motions of  $\sim 1.4$  mas yr $^{-1}$  (equivalent to a velocity of  $\sim 22$  km s $^{-1}$ ). This velocity is consistent with the proper motion values we have measured for the individual water maser features. This is more clearly seen from Figure 6, where we show as a close up the proper motions in the North-

ern and Southern bow-shock structures. The magnitudes of individual proper motions, represented by the arrow lengths, roughly coincide with the rate of increase in angular separation between the structures observed in 2001-2002 and those of 2008-2009. This is especially remarkable for the Southern bow-shock structure.

All these characteristics are consistent with the struc-

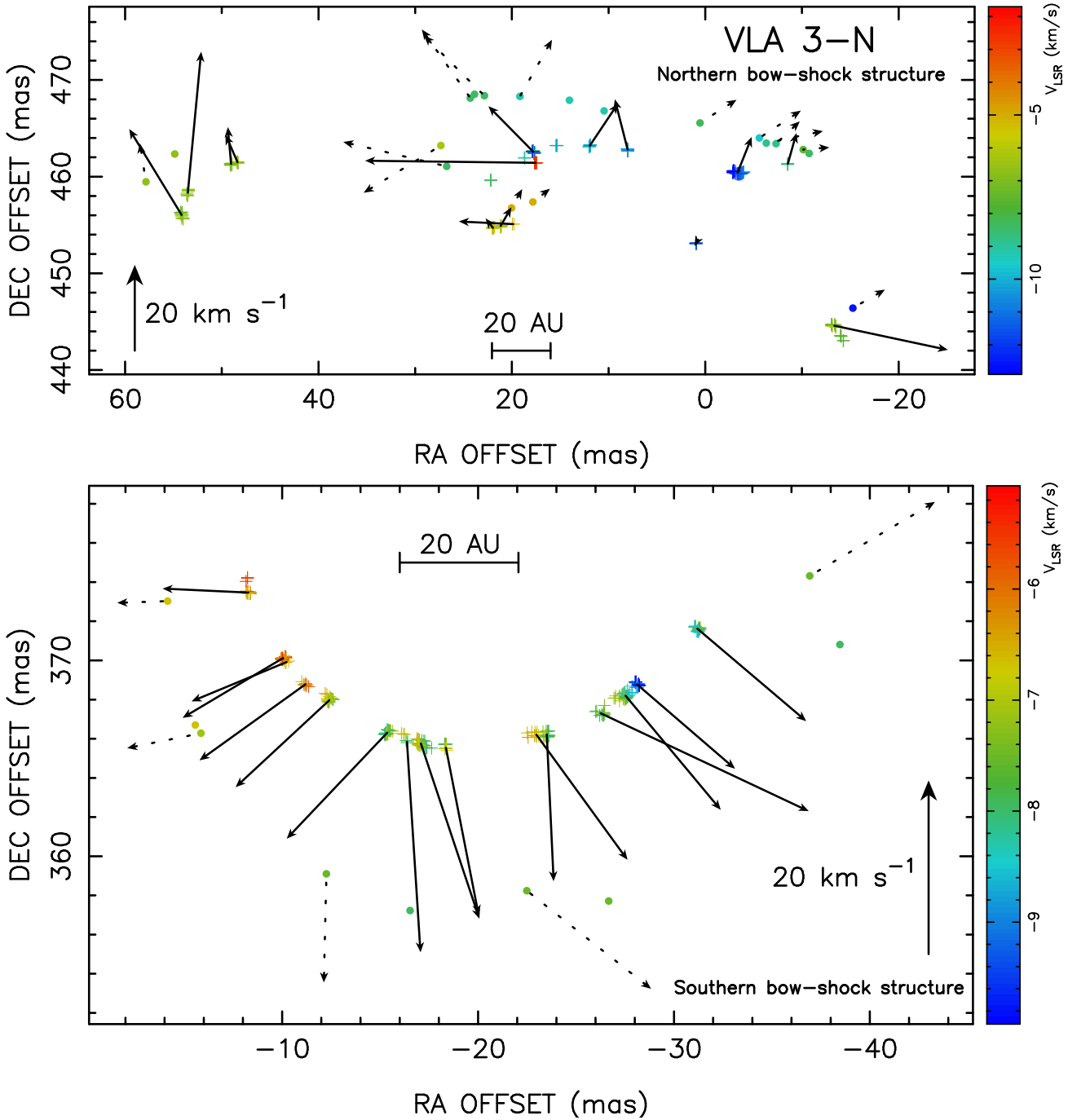


**Figure 6.** Same as in Figure 5, but showing a close up of the water maser proper motions of the Northern (top panel) and Southern (bottom panel) bow-shock structures in VLA 3-N. Note that the lengths of the solid arrows indicating the estimated shift in position for a time span of seven years roughly coincide with the angular separation between the structures observed in 2001-2002 (this paper) and those of 2008-2009 (Sanna et al. 2012), more noticeable for the Southern bow-shock structure. This is consistent with the structures moving at almost constant velocities during the time span of seven years.

tures moving at almost constant velocities during a time span of seven years. Considering that the difference between the radial velocities of the Northern and Southern bow-shock structures is a few  $\text{km s}^{-1}$  (Figure 4), and their radial velocities are relatively close to the radial velocity of the  $\text{HC}_3\text{N}$  line emission peak observed  $\sim 0.25''$  north from VLA 3 within the hot molecular core (Jiménez-Serra et al. 2012),

together with the large tangential velocities that we obtain ( $\sim 20 \text{ km s}^{-1}$ ), we conclude that the water masers structures in VLA 3-N are likely moving almost on the plane of the sky. In addition, within each of the two bow-shock structures, there are also small radial velocity differences. For the Southern bow shock, a small velocity shift of  $\sim 2 \text{ km s}^{-1}$  is observed, increasing west to east from  $V_{LSR} \simeq -8 \text{ km s}^{-1}$

**Table 1.** Proper motions of the VLBA water maser features in AFGL2591 VLA 3-N (2001-2002 epochs)

Feature ID	Detected Epochs	$V_{LSR}$ (km s <sup>-1</sup> )	Intensity (Jy beam <sup>-1</sup> )	$\Delta x$ (mas)	$\Delta y$ (mas)	$V_x$ (km s <sup>-1</sup> )	$V_y$ (km s <sup>-1</sup> )
1	1,2,3	-6.1	0.6	-8.27	373.46	9.8 ± 0.8	0.5 ± 0.6
2	1,2,3	-5.7	1.2	-10.05	370.12	11.6 ± 0.3	-6.9 ± 0.2
3	1,2,3	-6.5	0.1	-10.23	369.92	10.9 ± 0.2	-4.5 ± 0.3
4	2,3	-6.1	0.1	-11.19	368.78	12.2	-8.8
5	1,2,3	-7.1	0.4	-12.41	367.97	10.8 ± 1.3	-10.0 ± 1.1
6	1,2,3	-7.5	3.8	-15.37	366.31	11.6 ± 0.2	-12.2 ± 0.2
7	2,3	-7.8	1.5	-16.37	365.85	-1.6	-24.2
8	1,2,3	-7.3	4.3	-17.08	365.76	-6.7 ± 3.1	-20.2 ± 1.6
9	1,2,3	-7.3	1.7	-18.36	365.54	-3.8 ± 1.9	-19.2 ± 1.1
10	1,2,3	-6.7	0.3	-22.98	366.20	-10.5 ± 2.3	-14.4 ± 0.5
11	1,2,3	-7.4	0.8	-23.51	366.22	-0.8 ± 0.2	-16.9 ± 0.2
12	1,2,3	-7.7	0.4	-26.26	367.30	-23.9 ± 0.3	-11.3 ± 0.3
13	1,2,3	-8.0	6.6	-27.53	368.20	-10.9 ± 1.1	-13.1 ± 0.9
14	1,2,3	-8.9	5.1	-28.12	368.77	-11.3 ± 0.1	-9.7 ± 0.1
15	1,2,3	-8.0	2.8	-31.20	371.62	-12.5 ± 0.3	-10.6 ± 0.5
16	1,2,3	-7.3	0.7	-36.38	397.36	-4.8 ± 0.3	11.9 ± 0.3
17	2,3	-6.3	0.2	-30.78	434.50	12.2	0.3
18	1,2,3	-6.5	0.2	-30.88	435.01	7.7 ± 0.8	8.9 ± 1.7
19	1,2,3	-6.4	1.5	-13.36	444.58	-26.4 ± 0.9	-5.6 ± 0.2
20	1,2,3	-11.5	0.1	0.96	453.10	0.3 ± 0.2	-0.6 ± 0.3
21	1,2,3	-11.9	0.3	-3.35	460.43	-3.3 ± 1.7	8.3 ± 0.6
22	1,2,3	-8.7	0.5	-8.54	461.33	-2.0 ± 0.6	7.2 ± 1.3
23	1,2,3	-9.8	2.0	8.03	462.80	3.0 ± 0.2	11.7 ± 0.6
24	1,2,3	-9.1	4.3	11.94	463.19	-6.6 ± 1.1	9.8 ± 0.6
25	1,2,3	-9.0	20.6	17.78	462.57	10.5 ± 0.1	10.6 ± 0.6
26	2,3	-2.3	0.4	17.56	461.44	39.7	0.5
27	1,2	-5.2	0.1	19.86	455.09	12.7	0.6
28	1,2,3	-5.3	1.2	21.16	454.90	-2.5	4.4
29	1,2,3	-5.4	1.3	21.96	454.71	1.7 ± 0.1	2.2 ± 0.3
30	1,2,3	-6.5	0.7	48.37	461.49	2.8 ± 0.2	6.4 ± 0.2
31	1,2,3	-6.7	0.8	49.03	461.31	0.8 ± 1.9	8.6 ± 0.5
32	1,2,3	-6.8	0.1	53.52	458.35	-3.1 ± 1.6	32.8 ± 3.1
33	1,2,3	-6.7	0.4	54.16	456.04	12.2 ± 0.5	20.0 ± 0.8

**Notes.** The water maser features where proper motions have been measured are numbered in column 1 for identification purposes. For each feature, the different epochs of detection are given in column 2 (Epoch 1: 2001 Dec 02; Epoch 2: 2002 Feb 11; Epoch 3: 2002 Mar 05). Columns 3 and 4 give, respectively, the LSR radial velocity and peak intensity of the maser features as observed in the first epoch of detection. The position offset of the features (referred to the mean epoch of the epochs where the features are detected) are given in columns 5 and 6, while their proper motions are reported in columns 7 and 8. All the offset positions are relative to the maser spot position (0,0) used for self-calibrating the data of the first epoch, with absolute position RA(J2000) = 20<sup>h</sup>29<sup>m</sup>24.879<sup>s</sup>, DEC(J2000) = 40°11'19.47" (± 0.01") and  $V_{LSR} = -18.8$  km s<sup>-1</sup>. This maser spot used for self calibrating the data is associated with the radio continuum source VLA 3 (Trinidad et. al. 2003), ~ 0.5" south from the region subject of the study in this paper. For the alignment of the different observed epochs we used the maser feature S17 observed by Sanna et al. (2012) (see Table 2) and identified in our data set with maser feature ID 28 (this table), assuming it has constant velocity through the time span of ~ 7 years between our observations (2001-2002 epochs) and those of Sanna et al. (2008-2009 epochs). Consequently, for the maser feature ID 28, and for those detected only in two epochs (IDs 4, 7, 17, 26, and 27), there are not uncertainty estimates for the proper motion values (linear fitting). We estimate that the accuracy in the relative positions of the maser features is ~ 0.10 mas. The positions, LSR radial velocity, and intensity of all the maser spots observed in this region in the three epochs, are listed in Table A1 (published on-line; see §2) and represented in Figures 5 and 6.

to  $V_{LSR} \simeq -6$  km s<sup>-1</sup> (Figure 6). For the Northern bow shock, radial velocity differences are relatively larger than in the Southern one, up to ~ 4-5 km s<sup>-1</sup>, but these differences are distributed more irregularly.

#### 4 DISCUSSION: THE MASER SHELL AS A STELLAR WIND BOW SHOCK

The Northern and Southern shell-like structures traced by the water maser emission in VLA 3-N show systematic expanding motions that could imply one or two different centers of star formation activity. Here we consider two possible scenarios to explain the spatio-kinematical distribution of these masers: i) a static central source driving the two

**Table 2.** Proper motions of the VLBA water maser features in AFGL2591 VLA 3-N (2008-2009 epochs)

Feature ID	Detected Epochs	$V_{LSR}$ (km s <sup>-1</sup> )	Intensity (Jy beam <sup>-1</sup> )	$\Delta x$ (mas)	$\Delta y$ (mas)	$V_x$ (km s <sup>-1</sup> )	$V_y$ (km s <sup>-1</sup> )
S17	a,b,c,d	-5.0	22.2	20.04	456.77	-2.5 ± 1.8	4.4 ± 2.1
S18	a,b,c,d	-9.2	6.0	19.17	468.30	-7.5 ± 1.7	13.2 ± 2.0
S19	a,b,c,d	-12.6	5.4	-15.26	446.41	-7.5 ± 2.0	4.3 ± 2.5
S20	a,b,c,d	-7.5	4.5	-12.26	359.10	0.3 ± 2.2	-12.5 ± 2.4
S21	a,b,c,d	-8.8	2.9	-6.31	463.47	-13.2 ± 2.1	2.8 ± 2.1
S22	a,b,c,d	-8.8	2.3	-7.33	463.42	-5.5 ± 1.7	5.2 ± 2.0
S24	a,b,c	-8.4	2.0	24.30	468.13	11.3 ± 4.2	16.0 ± 4.3
S26	a,b,c,d	-7.5	1.6	-22.49	358.24	-14.3 ± 1.8	-11.3 ± 2.2
S28	a,b,c,d	-7.1	0.7	-5.86	366.28	8.5 ± 1.8	-1.7 ± 2.1
S30	a,b,c,d	-5.0	0.5	17.83	457.38	-4.0 ± 2.0	3.1 ± 2.0
S32	a,b,c,d	-8.3	0.4	0.54	465.56	-8.5 ± 1.8	5.4 ± 2.2
S33	a,b,c,d	-9.6	0.4	-5.59	464.00	-9.7 ± 2.1	6.4 ± 2.2
S34	a,b,c	-8.4	0.4	22.84	468.37	14.1 ± 3.3	14.0 ± 8.7
S35	a,b,c,d	-7.5	0.4	-36.93	374.32	-14.4 ± 1.8	8.5 ± 2.2
S36	b,c,d	-8.4	0.3	26.74	461.06	24.1 ± 3.0	5.7 ± 3.2
S37	a,b,c	-6.3	0.2	27.34	463.22	18.0 ± 3.3	-11.0 ± 4.7
S38	a,b,c,d	-6.7	0.2	57.85	459.46	1.4 ± 1.8	9.0 ± 2.2
S40	a,b,c,d	-6.7	0.2	-4.16	373.03	5.8 ± 1.8	-0.2 ± 2.1
S41	b,c,d	-7.5	0.2	-10.13	462.80	-6.1 ± 3.7	0.5 ± 3.0

**Notes.** Same as Table 1, but for the water maser features with proper motions measured by Sanna et al. (2012) for the epochs *a* (2008 Nov 10), *b* (2009 May 06), *c* (2009 May 13), and *d* (2009 Nov 13). The ID numbers of the features are the same as those listed by Sanna et al. (2012) preceded by an S. All the offset positions are with respect to the same (0,0) position given for the data of Table 1 after alignment of all the observed epochs (2001-2002 and 2008-2009; see notes in Table 1 and §2). In this way the offset positions listed in columns 5 and 6 of this table were obtained by adding (-631.01 mas, +151.08 mas) to the ( $\Delta x$ ,  $\Delta y$ ) positions listed in columns 5 and 6 of Table 2 of Sanna et al. (2012).

bow-shock structures; ii) two independent driving sources, one of them exciting the Northern bow-shock structure, and the other one, a young runaway star moving in the local molecular medium at  $\sim 20$  km s<sup>-1</sup>, exciting and molding the smoother Southern bow-shock structure. Given that the Southern structure has a remarkably smooth morphology and systematic proper motions, we use this structure to develop the model.

#### 4.1 The bow-shock model

The water masers of the Southern structure detected in the VLA 3-N region trace a more or less smooth arc on the plane of the sky. When compared with the structure observed by Sanna et al. (2012), it is clear that the arc-like structure (traced by the masers) is moving as a whole, in an approximately southward direction.

Sanna et al. (2012) interpreted this arc of masers, together with the Northern structure, as part of an elliptical bow shock expanding into the molecular cloud, driven by a static central source, and expanding into the molecular cloud. The heating and compression of the molecular material at the shock gives rise to the observed maser emission.

We think that this bow-shock interpretation is basically correct. But here we present a generalized and more detailed model for this bow-shock scenario. Our interpretation is based on the work of Raga et al. (1997) on the proper motions of condensations in a bow-shock flow. This work presents a derivation of the basic parameters of the bow shock (such as its velocity, direction and environmental mo-

tion) from a set of observed proper motions of water maser features.

Firstly, we assume that the bow shock has an axially symmetric shape and that it moves with a constant velocity (in magnitude and direction) with respect to the surrounding molecular cloud. As the bow shock moves, it heats, compresses and pushes the molecular cloud material, producing a thin shell of emitting gas.

The bow shock moves at a velocity  $v_{bs}$ , directed at an angle  $\phi$  with respect to the plane of the sky. The water masers are likely to trace the bow shock “edge” (i.e., the region in which the thin shell is tangential to the line of sight), since this is the line of maximum (local) optical depth as seen by the observer.

If we assume that the bow shock has a paraboloidal shape, the projection of the bow shock (which moves in an arbitrary direction) on the plane of the sky is also a parabola. This is demonstrated in Appendix A, in which we develop the equations describing the shape of the bow shock.

#### 4.2 Fits to the observed bow shapes

We now use equations (A8) to (A10) to carry out an unweighted least squares fit to the ( $x, y$ ) positions of the observed masers of the Southern structure (see Table A1), from which we obtain the parameters ( $x_0, y_0, \theta, B$ ) of the best-fit parabola. Fits are done to our three observed epochs, as well as to the 2008-2009 maser positions of Sanna et al. (2012).

The fits are shown in Figure 7, and the resulting parameters (together with their errors) are given in Table 3. As seen from the standard deviation of the values obtained

**Table 3.** Parameters of the parabolic fits to the bow shapes

Epoch	$t$ (days)	$x_0$ (mas)	$y_0$ (mas)	$\theta$ ( $^\circ$ )	$B$ ( $\text{mas}^{-1}$ )
1	0	-17.68	365.68	-9.73	0.0536
2	71	-17.64	365.44	-9.90	0.0532
3	93	-17.72	365.32	-9.45	0.0532
S <sup>1</sup>	2535	-19.50	356.56	-2.18	0.0530
$\sigma^2$	...	1.80	0.39	5.27	0.0038

<sup>1</sup> Sanna et al. (2012).<sup>2</sup> Standard deviations of the values obtained in the four parabolic fits.**Table 4.** Parameters of the bow shock for different orientations

$\phi$ ( $^\circ$ )	$R_0$ (AU)	$v_{bs}$ ( $\text{km s}^{-1}$ )	$R'_0$ (mas)
0	18.6	24.0	5.6
30	16.1	27.7	5.4
45	13.1	33.9	5.2
60	9.3	48.0	4.9
90	0.0	$\infty$	4.7

for each parameter in the fits of the different epochs, quoted in the bottom line of this table, the only parameters that show significant trends with time are  $x_0$  and  $y_0$  (i.e., the position of the head of the projected bow shock), while the dispersion of values of theta and B is small, consistent with a time-independent behavior.

In Figure 8 we plot the values of  $x_0$  and  $y_0$ ,  $\theta$  and  $B$  as a function of time. For  $x_0$  and  $y_0$  we have carried out least squares fits to the resulting time-dependencies (also shown in Figure 8), from which we obtain velocities

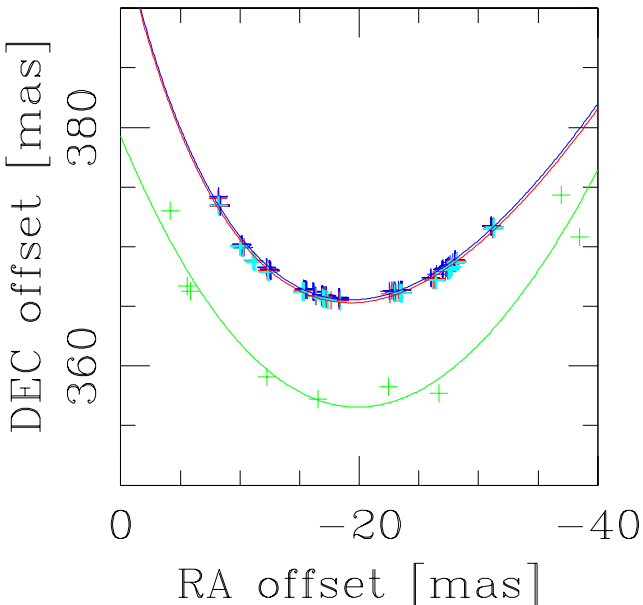


**Figure 7.** Maser positions from our three epochs (blue, magenta, and red crosses, see Table A1) and the maser positions from Sanna et al. (2012) (green crosses, see Table 2). The parabolic fits to the four sets of maser positions are shown with solid lines of the appropriate colours.

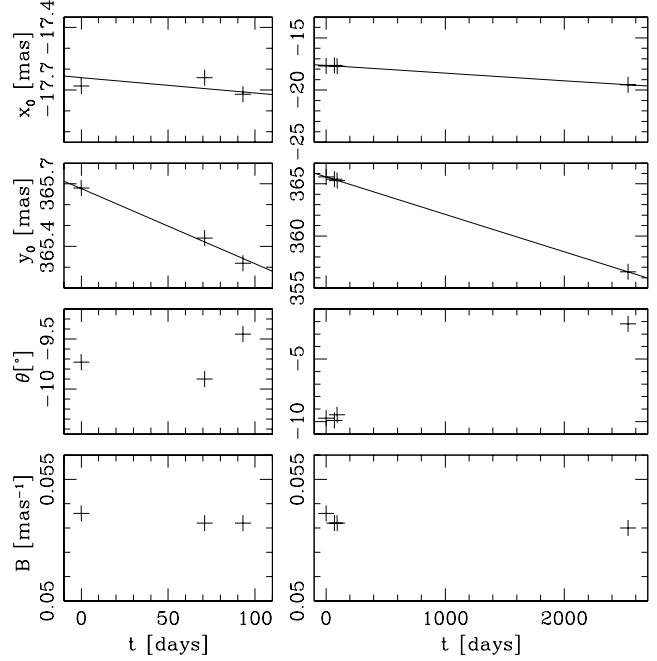


**Figure 8.** Parameters from the parabolic fits to the masers of our three epochs and the masers of Sanna et al. (2012) as a function of time (with  $t = 0$  corresponding to our first epoch: 2001 Dec 02). We have obtained linear fits for the position ( $x_0, y_0$ ) of the tip of the bow shock in the four available epochs, which are shown with solid lines in the corresponding plots (the same fits are shown in the plots of the left and right columns). The graphs of the right column show the four epochs, and the left column graphs show our three epochs with an expanded time-axis.

of  $(-0.27 \pm 0.31, -1.31 \pm 0.07) \text{ mas yr}^{-1}$  (in  $\alpha$  and  $\delta$ , respectively), corresponding to  $(-4.2 \pm 4.8, -20.6 \pm 1.0) \text{ km s}^{-1}$  at a distance of 3.3 kpc. The full plane of the sky velocity therefore is of  $21.0 \text{ km s}^{-1}$ , which is consistent with the proper motion velocities of the fastest masers (see Tables 1 and 2).

We have to note that a similar fit for the observed masers of the Northern structure is not possible because this structure shows a somewhat irregular morphology. However, we think that the nature of this structure is similar to that of the Southern bow shock and that the observed morphological differences could be due to a non uniform VLA 3-N ambient medium, being the density or turbulence larger in the northern parts. We also can not rule out that the Northern structure is more evolved and it has begun to disperse.

### 4.3 The motions of the individual masers

The motions of masers lying on the projected edge of a bow shock are also derived in Appendix A. We carry out least squares fits of equations (A15-A16) with  $B = 0.0533 \text{ mas}^{-1}$  and  $\theta = 9.7^\circ$  (the mean values of the fits to the bow shapes, see the right column of Table 3) to the observed  $v_{x'}$  and  $v_{y'}$  vs.  $x'$  dependencies, from which we obtain the parameters of the bow shock. The corresponding fits are shown in Figure 9. The parameters resulting from the  $v_{x'}$  vs.  $x'$  fit are:

$$v_{x'}^0 = -(2.95 \pm 1.32) \text{ km s}^{-1} \quad v_{bs} \cos \phi = (24.80 \pm 3.17) \text{ km s}^{-1}, \quad (1)$$

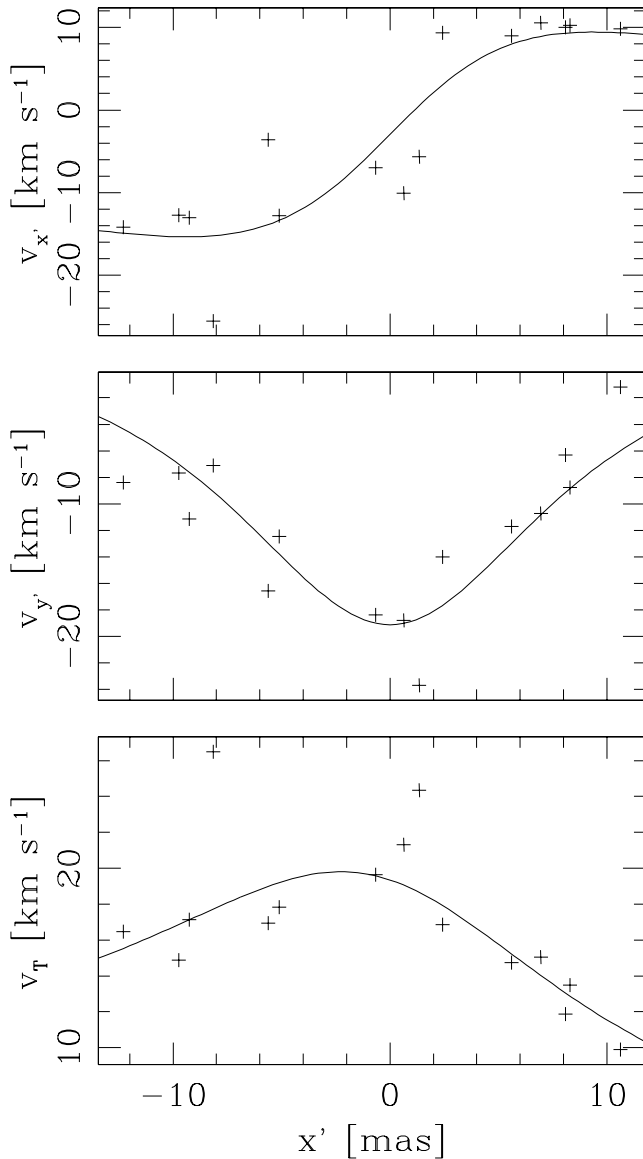


**Figure 9.** The crosses show the proper motions  $v_{x'}$ ,  $v_{y'}$  and  $v_T = \sqrt{v_{x'}^2 + v_{y'}^2}$  of the individual maser spots as a function of the  $x'$  coordinate (measured perpendicular to the axis of the projected bow shapes, see Figure A1). The solid lines correspond to the least squares fits described in the text.

and the parameters resulting from the  $v_{y'}$  vs.  $x'$  fit are:

$$v_{y'}^0 = (4.23 \pm 2.55) \text{ km s}^{-1} \quad v_{bs} \cos \phi = (23.35 \pm 3.55) \text{ km s}^{-1}. \quad (2)$$

The values of  $v_{bs} \cos \phi$  obtained from both fits are consistent. Also, using the inverted form of equations (A17) and (A18), from the fitted values of  $v_{x'}^0$  and  $v_{y'}^0$  (see equations 1-2), we obtain the motion on the plane of the sky

$$v_x^0 = (-3.62 \pm 2.72) \text{ km s}^{-1} \quad v_y^0 = (3.67 \pm 2.75) \text{ km s}^{-1}, \quad (3)$$

of the environment into which the bow shock is traveling. The  $(v_x^0, v_y^0)$  velocity corresponds to the motion of the molecular cloud with respect to the observer.

If we subtract this environmental motion from the velocity of the tip of the bow shock ( $-4.2$  and  $-20.6 \text{ km s}^{-1}$  along the  $x$  and  $y$  coordinates, calculated above from the fits

to the observed bow shapes), we obtain a  $(-0.57, -24.24) \text{ km s}^{-1}$  velocity (in  $\alpha$  and  $\delta$ , respectively) of the bow shock with respect to its surrounding environment. This corresponds to a full plane of the sky motion of  $24.25 \text{ km s}^{-1}$  of the bow shock with respect to the molecular cloud, which is consistent with the values of  $v_{bs} \cos \phi$  obtained from the fits to the  $v_{x'}^0$  and  $v_{y'}^0$  vs.  $x'$  dependencies (see equations 1 and 2).

In this way, we find that the proper motions derived from parabolic fits to the bow shapes (in the 4 different epochs) and the proper motions of the individual masers are all consistent with a single, parabolic bow shock model with a “shape parameter”  $B = 0.0533 \text{ mas}^{-1}$  (see equation A8) with a plane of the sky motion of  $(-0.6, 24.2) \text{ km s}^{-1}$  (along  $\alpha$  and  $\delta$ ) with respect to an environment with a  $(-3.6, 3.7) \text{ km s}^{-1}$  plane of the sky motion (see equation 3).

Now, if the maser spots are located in the leading edge of the projected bow shock, we expect their line of sight velocities to be zero. The observed small LSR velocity shift of the masers in the Southern bow-shock structure, with velocities between  $-8$  and  $-6 \text{ km s}^{-1}$  (see §3.1 and Table 1), therefore indicates that the environment molecular gas has radial velocities in this range. This result is in agreement with the millimeter CO and submillimeter  $\text{HC}_3\text{N}$  observations of van der Tak et al. (1999) and Jiménez-Serra et al. (2012), respectively.

#### 4.4 Parameters of the stellar wind: the runaway star scenario

The fact that the Northern and Southern bow-shock structures detected with our data present significant morphological differences, with the Southern one showing a remarkably smoother morphology, led us to consider an alternative scenario in which we have two embedded driving sources in VLA 3-N (instead of a single static central driving source). One exciting the most irregular Northern bow-shock structure, and the other one exciting the smoother Southern bow shock.

Let us now assume that the Southern bow shock is produced by the interaction of a spherical wind from a runaway star with a uniform molecular environment (while the Northern bow shock is produced by another different driving source). This problem has been studied, e.g., by Cantó et al. (1996), who give an analytic expression for the shape of the bow shock. This shape will remain unchanged as the star moves through the cloud, moving together with the star (consistent with the fact that the observed “shape parameter”  $B$  is approximately constant, see Table 3).

As mentioned above, the shape of the bow shock (close to its apex) can be approximated by the parabola given by equation (A4), with a stagnation radius  $R_0$  given by the ram pressure balance condition

$$\frac{\dot{M}_w v_w}{4\pi R_0^2} = \rho_0 v_*^2, \quad (4)$$

where  $\dot{M}_w$  and  $v_w$  are the wind mass loss rate and velocity (respectively),  $v_*$  is the velocity of the star with respect to the cloud and  $\rho_0$  is the environmental density. From equations (A3), (A4) and (A8) it follows that

$$R_0 = \frac{3 \cos \phi}{10B}. \quad (5)$$

Taking the  $B = 0.0533 \text{ mas}^{-1}$  value deduced from the observed bow shapes (see Table 3), we then obtain

$$\left(\frac{R_0}{\text{AU}}\right) = 18.6 \cos \phi, \quad (6)$$

for a distance of 3.3 kpc.

Now, from equations (1-2) we have

$$v_{bs} \approx \frac{24.0 \text{ km s}^{-1}}{\cos \phi}. \quad (7)$$

Also, the projected distance between the observed tip of the bow shock and the star is

$$R'_0 = |w'_0| + R_0 \cos \phi, \quad (8)$$

where  $w'_0$  is given by equation (A7). Using Eqs. (A8), (5) and (8), we obtain

$$R'_0 = \frac{1}{4B} \left(1 + \frac{1}{5} \cos^2 \phi\right), \quad (9)$$

or

$$\left(\frac{R'_0}{\text{mas}}\right) = 4.69 \left(1 + \frac{1}{5} \cos^2 \phi\right) \quad (10)$$

for  $B = 0.0533 \text{ mas}^{-1}$ . In Table 4, we give the values of  $R_0$ ,  $v_{bs}$  and  $R'_0$  for different values of the orientation angle  $\phi$  between the symmetry axis of the flow and the plane of the sky, obtained from equations (6), (7) and (10).

As expected, for  $\phi = 90^\circ$  there is no information about the bow-shock velocity. Interestingly, the position of the star with respect to the observed bow-shock tip ( $R'_0$ ) is limited to a range between 4.7 and 5.6 mas (for all values of  $\phi$ ). The narrowness of this interval is a consequence of the weak dependence of  $R'_0$  on the orientation angle  $\phi$  (see equation 9).

To estimate the stellar wind parameters, we have to fix a value for  $R_0$  and use equation (4). Let us take  $R_0 \approx 15 \text{ AU}$  and  $v_{bs} = 30 \text{ km s}^{-1}$  (corresponding to  $\phi \sim 37^\circ$ ), which are representative values for a bow shock with an angle  $\phi$  (with respect to the plane of the sky) not exceeding  $\sim 60^\circ$  (see Table 4). This velocity is highly supersonic with respect to the  $\leq 1 \text{ km s}^{-1}$  sound speed of the molecular cloud, and the shock is therefore strong.

Since in our model the shock velocity at the bow-shock tip is  $v_{bs} = v_*$ , the right hand side of equation (4) therefore represents the pressure in the cooling region of the shock. We then have

$$\rho_0 v_*^2 = \rho_0 v_{bs}^2 = nkT, \quad (11)$$

where  $n$  and  $T$  are the density and temperature of the cooling region (in which the maser emission is produced).

According to Claussen et al. (1997), the density  $n(H_2)$  of molecular hydrogen and the temperature  $T$  for the excitation of water maser emission at 22 GHz must be in the ranges  $n(H_2) \sim 10^8\text{-}10^9 \text{ cm}^{-3}$  and  $T \sim 200\text{-}300 \text{ K}$ . Therefore,  $nkT \sim (0.28\text{-}4.1) \times 10^{-5} \text{ dyn cm}^{-2}$ . We can then combine eqs. (4) and (11) to obtain:

$$\dot{M}_w v_w = 4\pi R_0^2 (nkT), \quad (12)$$

which for the parameters of our problem becomes

$$\left(\frac{\dot{M}_w}{10^{-8} M_\odot \text{ yr}^{-1}}\right) \left(\frac{v_w}{100 \text{ km s}^{-1}}\right) =$$

$$0.45 \left(\frac{R_0}{10 \text{ AU}}\right)^2 \left(\frac{nkT}{10^{-5} \text{ dyn cm}^{-2}}\right) \approx 0.28 - 4.1, \quad (13)$$

where the second equality corresponds to  $R_0 = 15 \text{ AU}$  and  $nkT \sim (0.28\text{-}4.1) \times 10^{-5} \text{ dyn cm}^{-2}$  (as estimated above). This result indicates that the observed maser arc could be produced by a young, low mass star with a wind velocity  $v_w \sim 100 \text{ km s}^{-1}$  and a moderate mass loss rate  $\dot{M}_w \sim 10^{-8} M_\odot \text{ yr}^{-1}$ .

Finally, let us estimate the density of the surrounding cloud. For this, we consider an average mass  $\bar{m} \approx 2m_H$  for the gas particles. From Eq. (11) we then obtain:

$$\left(\frac{n_0}{\text{cm}^{-3}}\right) = 3.0 \times 10^6 \left(\frac{nkT}{10^{-5}}\right) \left(\frac{10 \text{ km s}^{-1}}{v_{bs}}\right)^2 \approx (0.93 - 13.6) \times 10^5, \quad (14)$$

where for the second equality we have set  $v_{bs} = 30 \text{ km s}^{-1}$  and  $nkT$  in the range estimated above.

## 4.5 Summary

We find that the proper motions derived from parabolic fits to the observed Southern arc and the proper motions of the individual masers are consistent with a bow shock (with a time-independent shape) moving at a velocity of  $\sim 24 \text{ km s}^{-1}$  within an environment with a velocity of  $\sim 5 \text{ km s}^{-1}$  (both on the plane of the sky).

If we model this bow shock as the interaction of an isotropic stellar wind with a homogeneous, streaming environment, we find that the observations are consistent with a wind with a velocity  $v_w \sim 100 \text{ km s}^{-1}$  and a mass loss rate  $\dot{M}_w \sim 10^{-8} M_\odot \text{ yr}^{-1}$ . Therefore, the source producing the observed maser arc structure could be a normal low mass, young star, moving at a velocity of  $\sim 24 \text{ km s}^{-1}$  on the plane of the sky.

Interestingly, the stellar wind bow-shock model predicts that the position of the star should lie  $\approx 4.7 - 5.6 \text{ mas}$  approximately north of the apex of the bow shock (the range of possible distances corresponding to different possible values of the unknown angle  $\phi$  between the bow-shock axis and the plane of the sky). In an attempt to detect a radio continuum source at the predicted position by the model, we analyzed the VLA archive data of project AJ337. This project includes observations made in the A (2007 July 26), B (2008 January 18) and C (2008 March 09) configurations at 3.6 cm and 7 mm. The data were reduced following the NRAO recommendations and the different configurations were concatenated to obtain images of good quality. We clearly detect VLA 3 at both wavelengths, but we fail to detect a source towards VLA 3-N with 3- $\sigma$  upper limits of  $0.036 \text{ mJy beam}^{-1}$  ( $\lambda = 3.6 \text{ cm}$ ; beam  $\simeq 0.24''$ ) and  $0.20 \text{ mJy beam}^{-1}$  ( $\lambda = 7 \text{ mm}$ ; beam  $\simeq 0.15''$ ). Future searches with higher sensitivity of the emission from this source will show whether or not our bow-shock model works well in its present form.

It is important to note that a detailed model was not made for the water masers tracing the Northern bow-shock structure. As it has been mentioned, these masers are not showing a remarkably smooth morphology; instead, they are tracing an structure with a somewhat irregular morphology, opening the possibility that it is excited by another different YSO and in a possibly more turbulent region.

## 5 CONCLUSIONS

We have performed and analyzed multi-epoch VLBA water maser observations toward the high-mass star forming region AFGL 2591 with an angular resolution of 0.45 mas. Clusters of masers were detected toward the massive YSOs VLA2, VLA 3, and  $\sim 0.5''$  ( $\sim 1700$  AU) north of VLA 3, identifying a new center(s) of star formation by its outflow activity (VLA 3-N). The water maser emission in VLA 3-N is distributed in the form of two bow shock-like structures separated from each other by  $\sim 100$  mas ( $\sim 330$  AU). The Northern bow shock-like structure is moving essentially northward, while the Southern one is moving southward. These water maser structures observed in epochs 2001-2002 are contained within the area circumscribed by the corresponding structures observed by Sanna et al. (2012) in epochs 2008-2009, implying that these structures have persisted during the time span of seven years but increasing their angular separation at a relative proper motion of  $\sim 2.8$  mas yr $^{-1}$ . We find that, while the Northern bow shock-like structure has a somewhat irregular morphology, the Southern one has a remarkably smooth morphology. We have considered two alternative scenarios to explain these structures: (1) a single, static YSO ejecting a jet, and driving the two bow shock-like structures and (2) at least two YSOs, each of them exciting one of the structures.

In particular, we made a detailed modeling for the Southern structure and found that its spatio-kinematical distribution fits very well with a bow shock with a time-independent shape. We have modeled this bow shock as the interaction of an isotropic stellar wind from a runaway YSO with an homogeneous, streaming environment. The YSO moves at a velocity of  $\sim 24$  km s $^{-1}$  on the plane of the sky. Our model predicts that the position of this driving YSO (with  $v_w \sim 100$  km s $^{-1}$  and  $\dot{M}_w \sim 10^{-8} M_\odot$  yr $^{-1}$ ) should lie  $\sim 5$  mas north of the apex of the Southern bow shock.

Future, sensitive radio continuum observations are necessary to discriminate between the different scenarios, in particular to identify the still unseen driving source(s) and determine its (their) nature.

## ACKNOWLEDGMENTS

We would like to thank our referee for the very careful and useful report on our manuscript. GA, CC-G, RE, JFG, and JMT acknowledge support from MICINN (Spain) AYA2011-30228-C03 grant (co-funded with FEDER funds). JC and ACR acknowledge support from CONACyT grant 61547. SC acknowledges support from CONACyT grants 60581 and 168251. LFR acknowledges the support of DGAPA, UNAM, and of CONACyT (México). MAT acknowledges support from CONACyT grant 82543. RE and JMT acknowledge support from AGAUR (Catalonia) 2009SGR1172 grant. The ICC (UB) is a CSIC-Associated Unit through the ICE (CSIC).

## REFERENCES

- Armitage P. J. 2011, *ARA&A*, 49, 195  
 Bally J., Lada C. J. 1983, *ApJ*, 265, 824  
 Bally J., Zinnecker H. 2005, *AJ*, 129, 2281  
 Bartkiewicz A., van Langevelde, H. J. 2012, *IAU Symposium* 287, in press  
 Campbell B. 1984, *ApJ*, 287, 334  
 Cantó J., Raga A. C., Wilkin F. P. 1996, *ApJ*, 469, 729  
 Carrasco-González C., Galván-Madrid R., Anglada G., Osorio M., D'Alessio P., Hofner P., Rodríguez L. F., Linz, H., Araya E. D. 2012, *ApJ*, 752, L29  
 Carrasco-González C., Rodríguez L. F., Anglada G., Martí J., Torrelles J. M., Osorio M. 2010, *Science*, 330, 1209  
 Chibueze J. O., Imai H., Tafoya D., Omodaka T., Kameya O., Hirota T., Chong S., Torrelles J. M. 2012, *ApJ*, 748, 146  
 Claussen M. J., Marvel K. B., Wootten H. A., Wilking B. A. 1997, *IAUS*, 182, 515  
 Curiel S., Ho P. T. P., Patel N. A., et al. 2006, *ApJ*, 638, 878  
 Davies B., Lumsden S. L., Hoare M. G., Oudmaijer R. D., de Wit W.-J. 2010, *MNRAS*, 402, 1504  
 Doty S. D., van Dishoeck E. F., van der Tak F. F. S., Boonman A. M. S. 2002, *A&A*, 389, 446  
 Fernández-López M., Girart J. M., Curiel S., Gómez Y., Ho P. T. P., Patel N. 2011, *AJ*, 142, 97  
 Gallimore J. F., Cool R. J., Thornley M.-D. McMullin, J. 2003, *ApJ*, 586, 306  
 Goddi C., Moscadelli L., Sanna A. 2011, *A&A*, 535, L8  
 Goddi C., Moscadelli L., Torrelles J. M., Uscanga L., Cesaroni R. 2006, *A&A*, 447, L9  
 Hoare M. G., Franco J. 2007, in *Diffuse Matter from Star Forming Regions to Active Galaxies*, T.W. Hartquist, J. M. Pittard, and S. A. E. G. Falle (eds), Series A&SSP, 61  
 Hoare M. G., Kurtz S. E., Lizano S., Keto E., Hofner P. 2007, in *Protostars and Planets V*, B. Reipurth, D. Jewitt, and K. Keil (eds.), University of Arizona Press, Tucson, 181  
 Jiménez-Serra I., Martín-Pintado J., Rodríguez-Franco A., Chandler C., Comito C., Schilke P. 2007, *ApJ*, 661, L187  
 Jiménez-Serra I., Zhang Q., Viti S., Martín-Pintado J., de Wit W.-J. 2012, *ApJ*, 753, 34  
 Lada C. J. 1995, *Proceedings of the 7th Guo Shoujing Summer School on Astrophysics*, Yuan, C. and You, J. Editors, 1, 1  
 Lada C. J., Thronson H. A., Smith H. A., Schwartz P. R., Glaccum W. 1984, *ApJ*, 286, L302  
 Machida M. N., Inutsuka S.-i., Matsumoto T. 2008, *ApJ*, 676, 1088  
 McKee C. F., Ostriker E. C. 2007, *ARA&A*, 45, 565  
 Martí J., Rodríguez L. F., & Reipurth B. 1995, *ApJ*, 449, 184  
 Matthews L. D., Greenhill L. J., Goddi C., Chandler C. J., Humphreys E. M. L., Kunz M. W. 2010, *ApJ*, 708, 80  
 Meehan L. S. G., Wilking B. A., Claussen M. J., Mundy L. G., Wootten A. 1998, *AJ*, 115, 1599  
 Mitchell G. F., Maillard J., Hasewaga T. I. 1991, *ApJ*, 371, 342  
 Moscadelli L., Goddi C., Cesaroni R., Beltrán M. T., Furuya R. S. 2007, *A&A*, 472, 867  
 Patel N. A., Curiel S., Sridharan T. K., Zhang Q., Hunter T. R., Ho P. T. P., Torrelles J. M., Moran J. M., Gómez J. F., Anglada G. 2005, *Nature*, 437, 109  
 Raga A. C., Cantó J., Curiel S., Noriega-Crespo A., Raymond J. C. 1997, *RevMexAA*, 33, 157  
 Rygl K. L. J., Brunthaler A., Sanna A., Menten K. M., Reid

M. J., van Langevelde H. J., Honma M., Torstensson K. J. E., Fujisawa K. 2012, *A&A*, 539, 79

Sanna A., Moscadelli L., Cesaroni R., Tarchi A., Furuya R. S., Goddi C. 2010, *A&A*, 517, 71

Sanna A., Moscadelli L., Cesaroni R., Tarchi A., Furuya R. S., Goddi C. 2010, *A&A*, 517, 78

Sanna A., Reid M. J., Carrasco-González C., Menten K. M., Brunthaler A., Moscadelli L., Rygl K. L. J. 2012, *ApJ*, 745, 191

Stäuber P., Doty S. D., van Dishoeck E. F., Benz A. O. 2005, *A&A*, 440, 949

Surcis G., Vlemmings W. H. T., Curiel S., Hutawarakorn K. B., Torrelles J. M., Sarma A. P. 2011a, *A&A*, 527, 48

Surcis G., Vlemmings W. H. T., Torres R. M., van Langevelde, H. J., Hutawarakorn K. B. 2011b, *A&A*, 533, 47

Surcis G., Vlemmings W. H. T., van Langevelde, H. J., Hutawarakorn K. B. 2012, *A&A*, 541, 47

Tamura M., Gatley I., Joyce R. R., Ueno M., Suto H., Sekiguchi M. 1991, *ApJ*, 378, 611

Tofani G., Felli M., Taylor G. B., Hunter T. R. 1995, *A&AS*, 112, 299

Torrelles J. M., Patel N. A., Anglada G., Gómez J. F., Ho P. T. P., Lara L., Alberdi A., Cantó J., Curiel S., Garay G., Rodríguez, L. F. 2003, *ApJ*, 598, L115

Torrelles J. M., Patel N. A., Curiel S., Estalella R., Gómez J. F., Rodríguez L. F., Cantó J., Anglada G., Vlemmings W., Garay G., Raga A. C., Ho P. T. P. 2011, *MNRAS*, 410, 627

Torrelles J. M., Patel N. A., Curiel S., Ho P. T. P., Garay G., Rodríguez L. F. 2007, *ApJ*, 666, L37

Torrelles J. M., Patel N. A., Gómez J. F., Ho P. T. P., Rodríguez L. F., Anglada G., Garay G., Greenhill L., Curiel S., Cantó J. 2001a, *ApJ*, 560, 853

Torrelles J. M., Patel N. A., Gómez J. F., Ho P. T. P., Rodríguez L. F., Anglada, G. Garay G., Greenhill L., Curiel S., Cantó J. 2001b, *Nature*, 411, 277

Torrelles J. M., Rodríguez L. F., Cantó J., Marcaide J., Gyulbudaghian A. L. 1983, *RevMexAA*, 8, 147

Trinidad M. A., Curiel S., Cantó J., D’Alessio P., Rodríguez L. F., Torrelles J. M., Gómez J. F., Patel N., Ho P. T. P. 2003, *ApJ*, 589, 386

van der Tak F. F. S., van Dishoeck E. F., Evans II N. J., Bakker E. J., Blake G. A. 1999, *ApJ*, 522, 991

van der Tak F. F. S., Walmsley C. M., Herpin F., Ceccarelli, C. 2006, *A&A*, 447, 1011

Vlemmings W. H. T., Diamond P. J., van Langevelde H. J., Torrelles J. M. 2006, *A&A*, 448, 597

Vlemmings W. H. T., Surcis G., Torstensson K. J. E., van Langevelde H. J. 2010, *MNRAS*, 404, 134

Wilkin F. P. 1996, *ApJ*, 459, L31

Williams J. P., Cieza L. A. 2011, *ARA&A*, 49, 67

Zapata L. A., Ho P. T. P., Schilke P., Rodríguez L. F., Menten K., Palau A., Garrod R. T. 2009, *ApJ*, 698, 1422

Zinnecker H., Yorke H. W. 2007, *ARA&A*, 45, 481

## APPENDIX A: BOW SHOCK MODEL

### A1 The shape of the bow shock

Let  $r(w)$  be the cylindrical radius of the bow shock as a function of the distance  $w$  measured along the symmetry axis. Then, the locus of the edge of the bow shock on the  $(x', w')$  plane of the sky (with  $x' = 0$ ,  $w' = 0$  corresponding to the observed bow-shock tip, the  $x'$  axis perpendicular to the projected symmetry axis, and  $w'$  perpendicular to  $x'$ ) is given by (see Raga et al. 1997):

$$x' = r \left[ 1 - \left( \frac{dr}{dw} \right)^2 \tan^2 \phi \right]^{1/2}, \quad (\text{A1})$$

$$w' = w \cos \phi \left[ 1 - \frac{r}{w} \left( \frac{dr}{dw} \right) \tan^2 \phi \right]. \quad (\text{A2})$$

To proceed, let us assume that  $r(w)$  is a parabola:

$$r = Aw^{1/2}, \quad (\text{A3})$$

where  $A$  is a constant. We assume this shape for the bow shock because any “flat topped” functional form can be approximated to second order as a parabola in the region of its apex. For instance, a bow shock generated by a star with an isotropic wind moving into a uniform medium has a complex shape (Wilkin 1996; Cantó et al. 1996), which in the apex region can be approximated by

$$r = \left( \frac{10R_0}{3} \right)^{1/2} w^{1/2}, \quad (\text{A4})$$

where  $R_0$  is the distance between the star and the tip of the bow shock.

Combining equations (A1-A3), one can show that the locus of the edge of the bow shock on the plane of the sky is also a parabola, given by

$$x' = \frac{A}{\cos^{1/2} \phi} y'^{1/2}, \quad (\text{A5})$$

where

$$y' = w' - w'_0, \quad (\text{A6})$$

$$w'_0 = -\frac{A^2}{4} \tan \phi \sin \phi. \quad (\text{A7})$$

Actually,  $w'_0$  is the projected distance between the real tip of the bow shock and its “projected head” on the plane of the sky.

Now, if  $(x, y)$  is the observer’s reference frame (offsets in right ascension and declination with respect to a fiducial position), we have the general situation shown in Figure A1. From equation (A5), the shape of the bow shock on the plane of the sky is

$$y' = Bx'^2; \text{ with } B = \cos \phi / A^2. \quad (\text{A8})$$

Also, the  $(x', y')$  and the  $(x, y)$  reference frames obey the standard equations of coordinate transformation

$$x' = (x - x_0) \cos \theta - (y - y_0) \sin \theta, \quad (\text{A9})$$

$$y' = (x - x_0) \sin \theta + (y - y_0) \cos \theta, \quad (\text{A10})$$

where  $(x_0, y_0)$  are the coordinates of the head of the projected bow shock, and  $\theta$  is the angle between the projected symmetry axis and the  $y$ -axis (see Fig. A1).

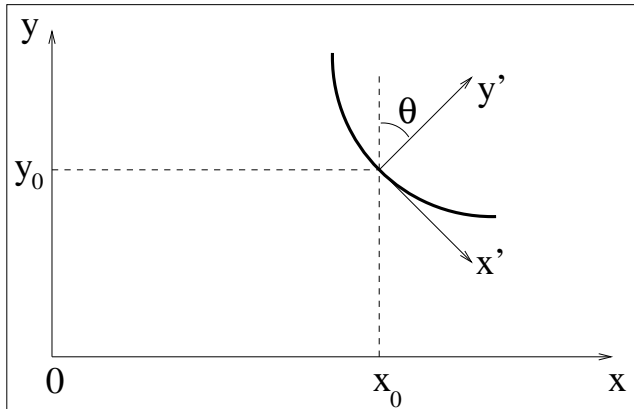


**Figure A1.** Schematic diagram showing the observer's plane-of-the-sky reference frame  $(x, y)$  and the  $(x', y')$  reference frame aligned with the projected bow shock shape (with the  $y'$  axis parallel to the symmetry axis of the bow shock, and  $y' = 0$  at the projected tip of the bow shock). The position on the plane of the sky of the projected bow-shock tip is  $(x_0, y_0)$ .

## A2 The velocity field

Let us now consider the motion on the plane of the sky of the post-bow shock gas. Let us first assume that the gas ahead of the bow shock is at rest. Following Raga et al. (1997), it is then straightforward to show that, locally, the gas moves in the direction of the vector normal to the shock. For a highly radiative shock, because of the large resulting compression of the material, the cooling region closely follows the motion of the shock. Therefore, the magnitude of its velocity is:

$$v = v_{bs} \sin \alpha, \quad (\text{A11})$$

where  $\alpha$  is obtained from the relation

$$\tan \alpha = \frac{dr}{dw}. \quad (\text{A12})$$

The projection of this velocity on the plane of the sky for the points along the observed edge of the bow shock is

$$v_{x'} = \pm v_{bs} \sin \alpha \cos \alpha \sqrt{1 - \tan^2 \alpha \tan^2 \phi}, \quad (\text{A13})$$

$$v_{y'} = -v_{bs} \frac{\sin^2 \alpha}{\cos \phi}, \quad (\text{A14})$$

while its projection along the line of sight is  $v_r = 0$ , consistent with the fact that we are seeing the edge of the bow shock, in which the line of sight is tangent to the bow-shock surface. The derivation of equations (A11-A14) is given by Raga et al. (1997; see their eqs. [16] and [17]).

Combining equations (A1), (A3), (A8), (A12), (A13) and (A14) one finds

$$v_{x'} = v_{x'}^0 + \frac{2Bx'}{1 + 4B^2x'^2} v_{bs} \cos \phi, \quad (\text{A15})$$

$$v_{y'} = v_{y'}^0 - \frac{v_{bs} \cos \phi}{1 + 4B^2x'^2}, \quad (\text{A16})$$

where we have also introduced  $v_{x'}^0$  and  $v_{y'}^0$ , which represent the two components of a possible motion (with respect to the observer) of the environment within which the bow shock is propagating.

Then, using equations (A9) and (A10) with  $x_0 =$

$-17.68\text{mas}$ ,  $y_0 = 365.48\text{mas}$  and  $\theta = -9^\circ.7$  (the average of epochs 1-3 of the parameters given in Table 3), we calculate the positions  $(x', y')$  from the maser positions of Table 1. Similarly, using the rotations

$$v_{x'} = v_x \cos \theta - v_y \sin \theta, \quad (\text{A17})$$

$$v_{y'} = v_x \sin \theta + v_y \cos \theta, \quad (\text{A18})$$

we obtain the  $v_{x'}$  and  $v_{y'}$  motions of the masers (in the primed reference system, aligned with the bow shock, see figure A1) from the observed proper motions given in Table 1. The resulting velocities as a function of the  $x'$  coordinate are shown in Figure 9. In this figure, we also plot the total velocity  $v_T = \sqrt{v_{x'}^2 + v_{y'}^2}$  on the plane of the sky.

This paper has been typeset from a  $\text{\TeX}/\text{\LaTeX}$  file prepared by the author.